

# Polarization of photoluminescence by optically driven orbital reconstruction in magnetically ordered CrCl<sub>3</sub>

Lanqing Zhou<sup>1,2</sup>, Marjana Ležaić<sup>3</sup>, Yuriy Mokrousov<sup>3,4</sup>, Minh N. Bui<sup>1,2</sup>, Renu Rani<sup>1,2</sup>, Detlev Grützmacher<sup>1,5</sup> and Beata E. Kardynał<sup>1,2\*</sup>

<sup>1</sup> Peter Grünberg Institute (PGI-9), Forschungszentrum Jülich, 52425 Jülich, Germany

<sup>2</sup> Department of Physics, RWTH Aachen University, 52074 Aachen, Germany

<sup>3</sup> Peter Grünberg Institute (PGI-1), Forschungszentrum Jülich, 52425 Jülich, Germany

<sup>4</sup> Institute of Physics, Johannes Gutenberg-University Mainz, 55128 Mainz, Germany

<sup>5</sup>Jülich-Aachen Research Alliance, Institute for Green-IT (PGI-10), Forschungszentrum Jülich and RWTH Aachen University, Germany

**KEYWORDS:** *Chromium Chloride, photoluminescence, polarization, ligand electronics*

## ABSTRACT

*In this paper, we show that photoluminescence from CrCl<sub>3</sub> bulk crystal exhibits a preferential polarization direction when films are magnetically ordered or strained. We verify the magnetization as responsible for the polarization by measuring the signal as a function of the temperature in Voigt configuration while applying the in-plane magnetic field. We show that phonon coupling contributing to vibronic transitions depolarizes the signal compared with zero phonon lines. We explain the data using DFT calculations, which reveal a magnetization-selective occupation of the low energy d-orbital triplet state of Cr<sup>3+</sup> upon photon absorption. In addition, the calculations find that the excitation of one electron results in the excited state acquiring out-of-plane components of spin and very large orbital magnetic moments, in addition to a lattice deformation.*

## INTRODUCTION

The potential of optical applications of antiferromagnetic (AFM) materials, such as information storage, has initiated growing interest in optical readout of the magnetic order.<sup>1</sup> On the other hand, the interplay of orbital degrees of freedom of electronic states with light attracts ever-growing attention. When a solid is subject to a perturbation by an electric field or a light pulse, the excited electronic states experience a modification in their orbital character by hybridization with other states. This process is often accompanied by currents originating in the spatial redistribution of the states and the corresponding formation of a non-equilibrium magnetization due to orbital moments, i.e., orbital magnetization. While in the d.c. domain, the aspects of corresponding orbital dynamics and currents of angular momentum are being intensively studied these days,<sup>2,3</sup> the intricate processes behind optically-generated orbital magnetization and its interplay with spin properties are very poorly understood. Recently, it was shown that exciting low-symmetry and magnetic materials with light can result in large currents of orbital angular momentum accompanied by THz emission and angular momentum accumulation.<sup>4-6</sup> The orbital magnetization by second-order processes can be sizeable.<sup>7,8</sup> On the other hand, achieving and detecting a drastic orbital modification of the transient electronic structure of a magnetic material, accompanied by a magnetization reorientation and colossal non-equilibrium orbital

---

\* b.kardynał@fz-juelich.de

moments, still remains a significant challenge.

Photoluminescence (PL) spectroscopy, while limited to specific classes of materials, provides a powerful technique for probing transient electronic structures and orbital dynamics in magnetic materials, as it provides direct insight into the energy levels and relaxation pathways of excited states. Its potential in getting insight into magnetic ordering has been recently demonstrated on layered NiPS<sub>3</sub>,<sup>9-11</sup> CrI<sub>3</sub>,<sup>12-15</sup> and CrBr<sub>3</sub>.<sup>16, 17</sup> In these examples, the polarization of light was linked to the spin of electrons. In contrast to CrI<sub>3</sub> and CrBr<sub>3</sub> with an out-of-plane magnetic ordering, each CrCl<sub>3</sub> monolayer (ML) is magnetized in the plane of the Cr sub-lattice. The magnetic order develops from the high temperature paramagnetic (PM) phase in two steps; MLs enter the ferromagnetic (FM)-like phase at 17 K, and AFM coupling between them develops upon further cooling to 14.5 K.<sup>18</sup> As a result, in contrast with CrI<sub>3</sub> and CrBr<sub>3</sub>, the PL of CrCl<sub>3</sub> does not exhibit circular dichroism.<sup>19</sup> Until now, no effect of magnetization on the properties of excitons in CrCl<sub>3</sub> has been reported.

Here, we show that photoluminescence from CrCl<sub>3</sub> crystal collected along the c-axis is emitted with a preferential polarization direction related to the in-plane magnetization of the CrCl<sub>3</sub> MLs, which we introduce by applying a magnetic field. Further, we distinguish this effect from the polarization introduced by the strain by measuring the polarization at different temperatures. We explain the data with *ab-initio* calculations as resulting from breaking orbital symmetry in the magnetized CrCl<sub>3</sub> upon electron excitation. We predict that the interaction of CrCl<sub>3</sub> electrons with laser pulse drives the system into a transient state with a very large orbital moment in addition to non-vanishing spin magnetization. Our findings thus provide evidence for colossal orbital response to light driven. This opens possibilities for applications in opto-orbitronics, where orbital generation and relaxation on a sub-ps scale can result in prominent orbital transport and magnetization dynamics.

## EXPERIMENTAL DATA

Figure 1(a) shows a typical polarization-resolved photoluminescence (PL) from the CrCl<sub>3</sub> at 2 K excited by a laser at 1.8 eV (Sketch of setup in Figure S1). The two spectra in the figure were measured along orthogonal linear polarization directions. Both spectra are dominated by the broad peak between 1.3 and 1.6 eV, characteristic of vibronic optical transitions between crystal-field split Cr<sup>3+</sup> d-orbitals. A weak zero phonon line (ZPL) can be seen at 1.575 eV and enlarged in the inset. The preferred polarization direction can be seen in the entire wavelength range, including the ZPL. In the remaining text, we analyze the vibronic signal (counts integrated over the whole CrCl<sub>3</sub> emission energy range) and ZPL (an area under the Gaussian line fitted to the data in the ZPL energy range) signal.

Vibronic and ZPL signals as a function of polarization angle in Figure (b, c) show the polarization of the PL is independent of the excitation polarization. This means there is no linear dichroism in the absorption at 1.8 eV, and PL polarization is unrelated to the spin generated by absorption. The lowest energy, optically bright excitons in CrCl<sub>3</sub> are composed of an electron in the e<sub>g</sub> doublet and two electrons (and a hole) in the t<sub>2g</sub> triplet on the d-orbital of the Cr<sup>3+</sup> ion. Without symmetry breaking, the hole is equally likely to occupy any of the t<sub>2g</sub> triplet states (see diagram in Figure S2), and even though excitons are directional,<sup>20, 21</sup> on average, ZPL should be unpolarized. The symmetry can be broken by ML magnetization and uniaxial in-plane strain, which can be easily introduced.<sup>12, 13, 22</sup> Both magnetization and strain can also affect phonon and magnon dispersions, contributing to vibronic emission. To gain insight into the role of these two factors on the observed polarization, we measured the samples in the temperature range from above Néel temperature (17 K) of bulk CrCl<sub>3</sub> to 2 K.

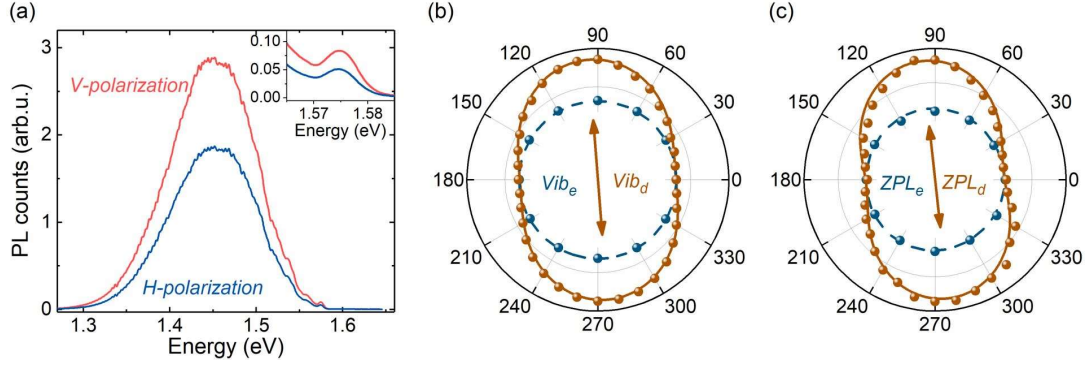


Figure 1. (a) Photoluminescence spectra from CrCl<sub>3</sub> collected at vertical (V) and horizontal (H) polarizations with horizontally polarized laser at 1.8eV. The ZPL region is shown in the inset. (b) An integrated vibronic PL and (c) a ZPL signal as a function of polarization detection and laser polarization angles, with H defined along a 0-180° line. Brown symbols ( $Vib_d$ ,  $ZPL_d$ ) show integrated PL measured at different polarization detection angles with fixed excitation polarization at H. Blue symbols ( $Vib_e$ ,  $ZPL_e$ ) show the H polarization component of PL as a function of the excitation-beam polarization. Solid lines are fitted curves using a  $\cos^2\theta$  function.

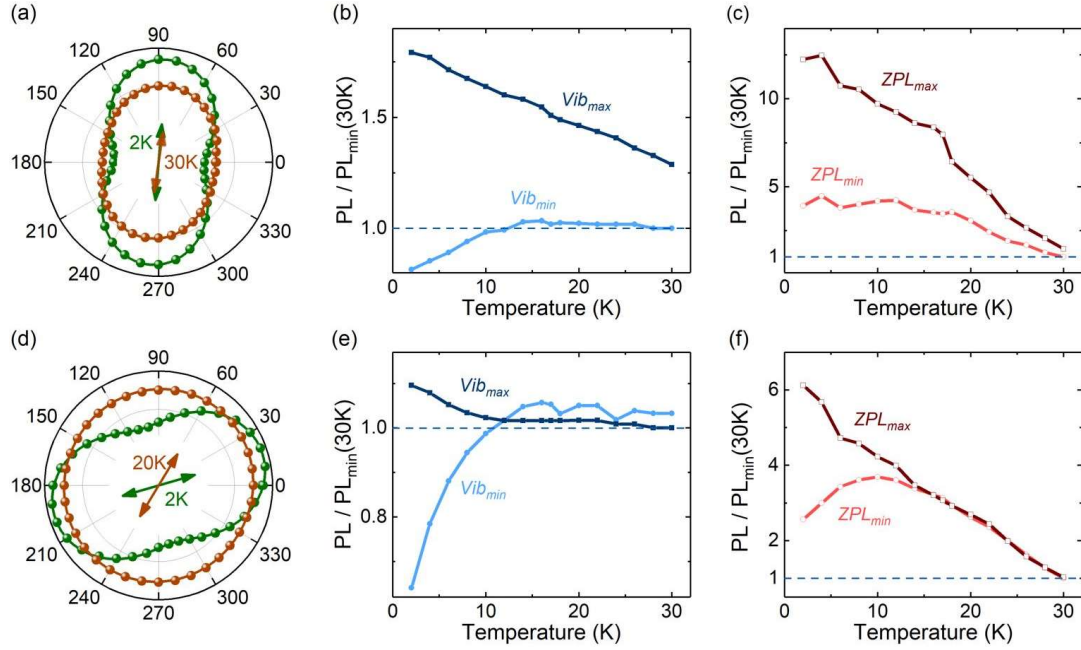


Figure 2. Evolution of photoluminescence integrated counts with the temperature for two representative cases (sample spots). (a-c) PL polarization is present even at 30K for some locations (d-f) and is vanishing above Néel temperature for other ones. (a,d) show integrated PL counts as a function of polarization angle below and above the Néel temperature (17 K), arrows show that the preferred polarization axis stays almost unchanged in (a) but rotates in (d). Solid lines are fitted curves using a  $\cos^2\theta$  function. Variations of vibronic (b,e) and ZPL (c,f) signals at two polarization directions, selected to point along ( $Vib_{max}$ ,  $ZPL_{max}$ ) and perpendicular ( $Vib_{min}$ ,  $ZPL_{min}$ ) to the direction of polarization at 2K in (a) and (d), respectively. The data is normalized to the minimum value at 30 K. Because of the polarization rotation and fixed polarization basis aligned with the vibronic signal at 2 K when acquiring data for Figure 2(e-f), the true  $Vib_{max}$  and  $ZPL_{max}$  change more, and  $Vib_{min}$  and  $ZPL_{min}$  less than the figures suggest.

The vibronic signals as a function of linear polarization detection angle at 30 K and 2 K, which are

above and below the Néel temperature (17K), are shown in Figure 2(a). The temperature-dependent measurement of its two polarization components (along ( $Vib_{max}$ ) and orthogonal ( $Vib_{min}$ ) to the preferred polarization direction at 2K) in the temperature range between 2 K and 30 K is plotted in Figure 2(b). The data is normalized to  $Vib_{min}$  at 30 K. An equivalent plot for ZPL is shown in Figure 2(c). Both vibronic and ZPL signals exhibit preferential polarization direction in the whole temperature range, and the preferred polarization orientations of vibronic and ZPL signals are almost the same at 30 K and 2 K (Figure S3 for ZPL), suggesting strain as the dominant origin of the observed polarization. Since strain lifts  $t_{2g}$  degeneracy,<sup>12, 23, 24</sup> electrons occupy preferentially the lower energy states subject to the weaker crystal field.

The two orthogonal polarization components of the ZPL signal ( $ZPL_{max}$  and  $ZPL_{min}$ ) increase in integrated counts upon cool-down; thus, these optical transitions are allowed by the static crystal field. The temperature evolution of these two components is, however, different.  $ZPL_{max}$  increases smoothly across the phase transitions temperature range (14.4 - 17 K) upon cool down. At the same time, the weaker one ( $ZPL_{min}$ ) saturates below approximately 18 K.  $Vib_{max}$  and  $Vib_{min}$  also follow different trends upon cool down (Figure 2b).  $Vib_{max}$  increases monotonically from 30 K to 2 K. In contrast,  $Vib_{min}$  doesn't change much when the sample is cooled down from 30 K to 15K and then sharply decreases. We define the degree of polarization (DoP) as  $\frac{I_{max}-I_{min}}{I_{max}+I_{min}}$ , where  $I_{max}$ ,  $I_{min}$  are the integrated luminescence counts measured with the analyzer along and orthogonal to the preferential polarization direction. The vibronic signal DoP is higher at 2 K (39.1%) than at 30 K (15.2%). Both are smaller than the respective values (55.1% at 2 K and 18.7 % at 30 K) for ZPL. Since the polarization direction of PL is almost the same at 30 K and 2 K, vibronic coupling depolarizes the electronic transitions.<sup>16</sup> Different temperature evolutions of  $Vib_{max}$  and  $Vib_{min}$  corroborate the complex vibronic coupling. This means electronic excitations that decay into photons with different polarizations couple differently to phonons or magnons. The change of the trends around magnetic phase transitions indicates that both electronic states and vibronic coupling may depend on spin orientation.

Figure 2(d-f) summarizes another behavior observed in the measurements (see also Figure S4) with the DoP of the vibronic/ZPL negligibly small (absent) above 14 K. Several features of the data are similar to that in Figure 2(a-c).  $Vib_{max}$  and  $ZPL_{max}$  increase upon cool down,  $Vib_{min}$  decreases from around Néel temperature, and the PL becomes more polarized. However, unlike in Figure 2(a), the polarization direction of the vibronic signal is different at 20 K and 2 K (Figure 2(d)). Its gradual rotation with temperature decreasing from 12 to 2 K is shown in Figure S5.

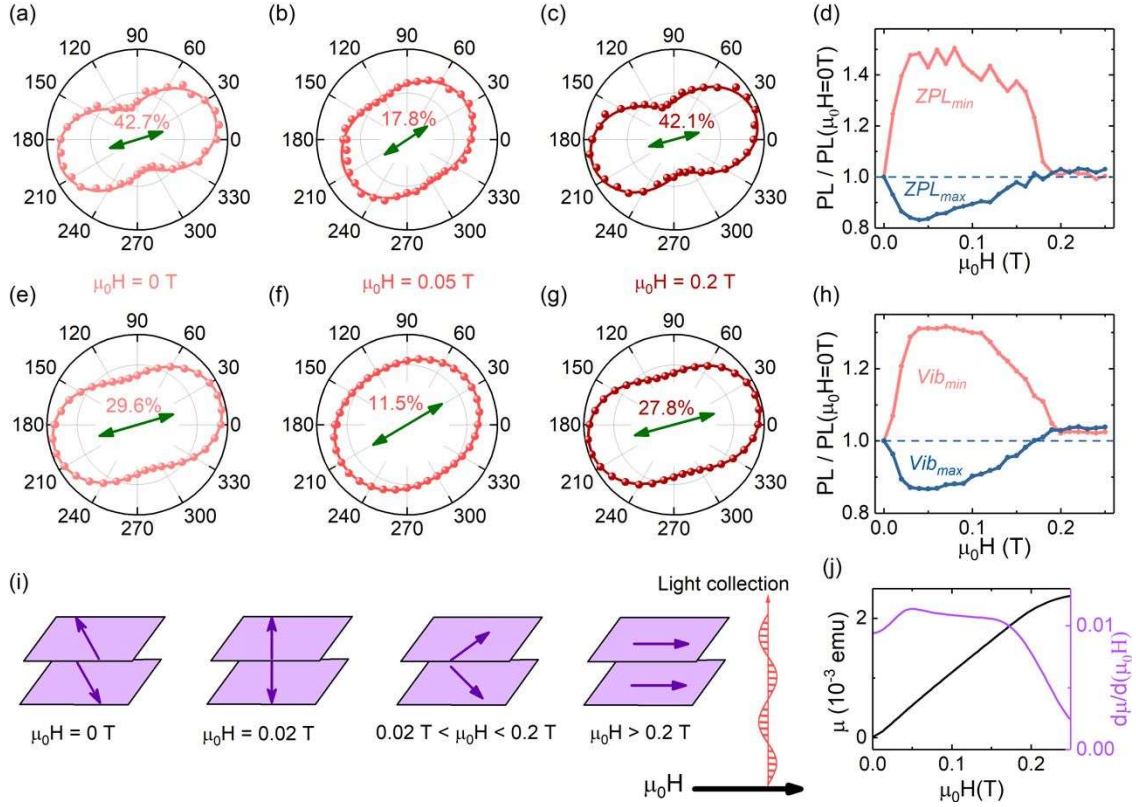


Figure 3. (a-c) Polar plots of polarization-resolved ZPL signal at 0, 50, and 200 mT, respectively, at a position where polarization occurs only below Néel temperature, shown on the same radial scale. Solid lines are fitted curves using a  $\cos^2\theta$  function. Green arrows mark the preferred polarization direction. The DoP is given above the arrow. (d)  $ZPL_{max}$  and  $ZPL_{min}$  measured along and perpendicular to the arrow in (a) as a function of the applied magnetic field. ZPL signals are normalized to their zero-field value. (e-h) show equivalent data for the vibronic signal. (i) Schematic diagram of spin reorientation in  $\text{CrCl}_3$  with an in-plane magnetic field. (j) Magnetization curve (black) measured at 2.5 K and its first derivative curve (purple).

The appearance of polarization below the reported PM-FM phase transition temperature in Figure 2(d) and the evolution of the vibronic and ZPL signal in Figure 2(e-f) point to a correlation between PL polarization and spin order. The in-plane spin orientation can be manipulated with a magnetic field in the  $\text{CrCl}_3$  ML plane. The polar plots in Figure 3(a-c) show polarization resolved ZPL measured in Voigt geometry at  $\mu_0H = 0, 50,$  and  $200$  mT applied along  $0-180^\circ$ . The corresponding evolutions of two orthogonal components of polarization, measured in the bases of the vibronic signal at  $\mu_0H = 0$  T, from  $0$  T to  $250$  mT, are shown in Figure 3(d). The equivalent data for the vibronic signal is shown in Figure 3(d-h). As can be seen from Figure 3(a), the ZPL DoP is  $42.7\%$ , and the maximum signal is measured at  $17^\circ$  from the horizontal when no external field is applied. At  $50$  mT (Figure 3(b)), the polarization points along  $33.6^\circ$ , and its DoP drops to  $17.8\%$ . When the applied field reaches  $200$  mT (Figure 3(c)), the DoP returns to  $42.1\%$  and points along  $15.2^\circ$ . The polarization of the vibronic signal (Figure 3(e-g)) undergoes similar changes, but the polarization axes are slightly different, and DoP is visibly lower. According to the evolution of two orthogonal components of polarization (Figure 3(d, h)), the highest polarization changes occur between  $0$  and  $20$  mT and then between  $100$  and  $200$  mT. Between  $200$  mT and  $250$  mT, both vibronic and ZPL signals saturate. The data follows the spin rotation

process in Figure 3(i) [19, 20] and can be compared with the magnetization curve in Figure 3(j) (Temperature-dependent magnetization curve in Figure S6). The magnetization changes only very weakly up to 20 mT and visibly up to 200 mT. Figure 3 is typical for spots with low DoP at high temperatures; another example can be seen in Figure S7.

The magnetic-field evolution of luminescence from the location of high DoP above Néel temperatures (Figure 2(a)) is shown in Figure 4. The polar plots and evolution of two orthogonal components with magnetic field are shown in Figure 4(a-d) for ZPL and Figure 4(e-h) for vibronic signal. There is negligible polarization rotation of the signals in the applied field range; only a slight decrease of DoP from 50 mT to 200 mT can be seen.  $Vib_{max}$  and  $ZPL_{max}$  keep constant with the magnetic field, and  $Vib_{min}$  and  $ZPL_{min}$  slightly increase, starting at 200 mT, as illustrated in Figure 4(d, h).

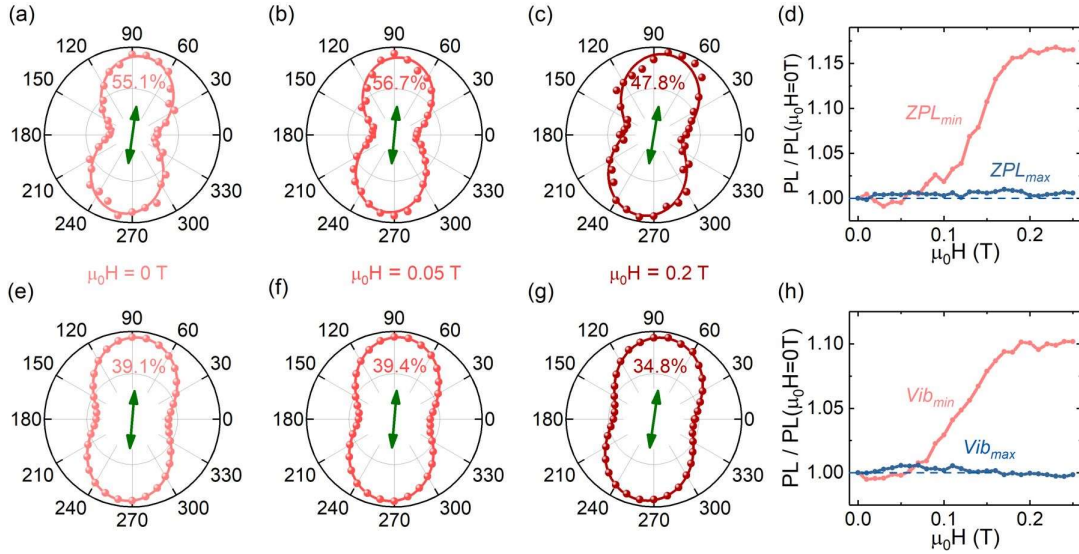


Figure 4. Magnetic field dependence of polarization-resolved PL for a region where polarization still exists above Néel temperature with high DoP. (a-c) Polar plots of the polarization dependence of ZPL at 0, 50mT, and 200mT on the same radial scale. Green arrows point in the direction of preferred polarization. The DoP is given above the arrow. (d) The evolution of ZPL signal in directions of maximum and minimum in (a) with increasing magnetic field. ZPL values are normalized to the zero-field ones. (e-h) equivalent plots for the vibronic signal. The polarized direction for ZPL at 0, 50mT and 200mT are  $82.4^\circ$ ,  $84.7^\circ$  and  $80.4^\circ$ . The polarized directions for the vibronic peak are  $85.2^\circ$ ,  $85.1^\circ$  and  $82^\circ$ . The weak effect of the magnetic field suggests the splitting of the levels caused by strain is dominant in this field range.

## Discussion and Simulations

The energetic ordering of electronic states of  $Cr^{3+}$  in distorted octahedra of Cl-ligands (see Supplementary Information) and the ground state of the ion are well understood.<sup>12, 13, 15, 24</sup> Here, we would like to elaborate on the effect of magnetization on the fine structure of the excited state, which manifests itself in PL polarization.

To simulate an excited state of  $CrCl_3$ , we employed the Vienna Ab-initio Simulation Package (VASP)<sup>25-28</sup> and performed calculations of the ferromagnetically ordered crystal ML using a unit cell that contains eight formula units. The Cr magnetic moments were aligned along the crystallographic axis (see axes orientation in Figure 5), which we find to be the easy magnetization axis in the ground state. For computational details, please see the Supplemental Information.

We find that in the ground state, when all  $d$  electrons reside in  $t_{2g}$  bands, the magnetic spin moment

per  $\text{Cr}^{3+}$  ion is  $(2.81, 0.0, 0.0)\mu_{\text{B}}$ , which is close to the  $3\mu_{\text{B}}$  expected for three electrons with aligned spins.<sup>18, 29</sup> The orbital magnetic moment is found to be  $(-0.03, 0.0, 0.0)\mu_{\text{B}}$ , consistent with expected quenching in the octahedral crystal field of  $\text{Cl}^-$  ligands. The excited state of a  $\text{Cr}^{3+}$  ion was simulated in the supercell by moving one electron from the  $t_{2g}$  to the  $e_g$  band, in the fixed-state-occupation mode of VASP. The hole in the  $t_{2g}$  states and the corresponding electron in the  $e_g$  states localize on one of the eight  $\text{Cr}^{3+}$  cations in the supercell, yielding a magnetic spin moment of  $(2.79, 0.04, -0.88)\mu_{\text{B}}$  and the orbital magnetic moment of  $(-0.55, 0.05, -0.5)\mu_{\text{B}}$  for this cation.

The large orbital moment, pointing along one of the  $\text{Cr}^{3+}$ -Cl bonds (thus having components along the  $a$ -axis as well as out-of-plane), is a consequence of the hole occupying the state, which is a linear combination of the  $t_{2g}$  states of the  $\text{Cr}^{3+}$  ion, with the characteristic charge distribution shown in Figure 5(a). The difference between the charge distributions of the simulated excited state and the ground state of the system is shown in Figure 5(b). Clearly, the excitation breaks the initial symmetry of the hexagonal lattice present at the ground state. The subsequent atomic relaxations result in a contraction of the bond length between the excited  $\text{Cr}^{3+}$  ion and its first  $\text{Cr}^{3+}$  neighbor that is still in its ground state in the direction perpendicular to the magnetization. This leads to a monoclinic unit cell for the excited state.

Recent DFT simulations of light absorption in  $\text{CrCl}_3$  concluded that the excited electron is partially delocalized and extending symmetrically towards two  $\text{Cl}^-$  ions.<sup>20</sup> However, no change in the absorption spectrum with the magnetic order of the ML was predicted for these low-energy photons. The comparison of these findings with our results implies that simulations of PL need to start from the atomic configuration of the excited state.

The simulations do not consider the excitation of random cations, which will occur in experiments. However, our conclusions apply to a sample uniformly magnetized along the crystallographic  $a$ -axis. Since the spin moment of an ion is aligned with the magnetic spin moments on the surrounding  $\text{Cr}^{3+}$  sites, the monoclinic distortion around the randomly excited  $\text{Cr}^{3+}$ -cations has the same orientation throughout the magnetic domain.

The laser spot size of the order of one micrometer and depth of focus of several monolayers in our optical measurements give a spatial resolution limit for domain sizes that can lead to photon polarization. Since our experiment shows magnetization-related changes near the paramagnetic-ferromagnetic phase transition, some larger (but local) domains of the same magnetization direction must already be present in the samples at this temperature.

It should be noted that a hole in the excited state gains an out-of-the-plane spin and orbital moment component. Refilling this state with an electron during radiative recombination creates a spin defect in the sea of aligned spins of the  $\text{Cr}^{3+}$  sub-lattice. Relaxation of that spin is likely to generate a magnon whose properties would be linked to the direction of magnetization and entangled with the generated photon. This also means that ZPL does not originate from a purely electronic transition but one accompanied by a generation/annihilation of a magnon.

Having established the effect of magnetization of the  $\text{CrCl}_3$  on the spin distribution in  $\text{Cr}^{3+}$ , we can compare the PL in Figure 3 (a-h) with the magnetization curve in Figure 3(j). As sketched in Figure 3(i), sample remagnetization occurs in two steps when an external magnetic field is applied along the spin orientation in the AF phase.<sup>30, 31</sup> At 20 mT, the spins in each ML “flop” in the plane to the direction normal to the applied magnetic field while each ML remains in FM order. Further increase of the magnetic field rotates the spins towards the external field until they are aligned with the external field above 200 mT (Figure 3(j)). The steps are reproduced in Figure 3(d), with the flop at 20 mT resulting in rapid changes in counts of the two polarizations. The return to the zero-field magnetization at 150 mT is consistent with the axes of polarizations pointing in similar directions. The differences between

Figure 3(d) and 3(j) can result from the rotation of the polarization axis, which was recorded only at discrete magnetic fields (Figure 3(a-c)). Above 200 mT, the polarization axis is  $17^\circ$  rotated compared with the expected value. Currently, we have no explanation for this finding. Considering that the rotation of the polarization axis in Figure S7 is  $20.6^\circ$ , it could be a sign of strain still present in samples. However, further studies are needed to understand the discrepancy between the expected and experimental polarization angle above 200 mT.

Figure 4 clearly shows the impact of strain. We would expect a gradual rotation of the spin orientation for the magnetization-induced PL polarization since zero-field polarization is perpendicular to the external field. The weak effect of the magnetic field suggests that the strain-induced energy level splitting is dominant at this point.

It is also worth noticing that the current insight into the origin of polarization also applies to disordered or defective  $\text{CrCl}_3$ . Local, random lattice distortions may contribute to the depolarization of the PL. Lattice defects, e.g., Cl vacancies or oxygen in Cl sites, are unlikely to cause polarization as they are randomly distributed in the lattice.

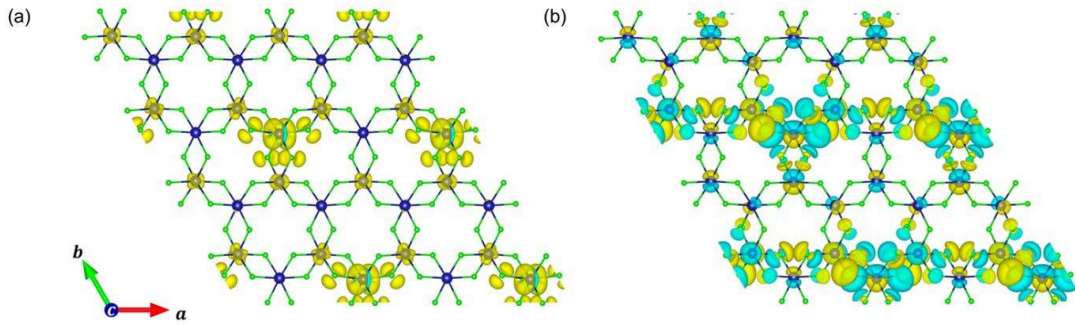


Figure 5: Ab-initio calculated spatial charge-distributions obtained for eight formula-unit large computational unit cells, when one of the three occupied  $t_{2g}$  electrons is placed in the unoccupied  $e_g$  state. Dark blue (light green) spheres represent  $\text{Cr}^{3+}$  ( $\text{Cl}^-$ ) ions. (a) Spatial charge distribution of the hole in the  $t_{2g}$  band of magnetically ordered  $\text{CrCl}_3$  monolayer, with spins pointing along the crystallographic axis  $a$ . (b) Difference in the spatial charge distribution of the occupied bands in the state containing the electron-hole pair and the ground state of the system, showing the local reduction of the symmetry to the monoclinic one. Yellow (light blue) surfaces show the regions where the difference is positive (negative). VESTA code<sup>32</sup> was used to plot the data.

## CONCLUSIONS

We have shown that photoluminescence from  $\text{CrCl}_3$  shows preferential polarization direction as a result of symmetry breaking by magnetization and also an in-plane uniaxial strain. The latter manifests as light polarization above Néel temperature, the former as a rapid increase of polarization degree below Néel temperature, accompanied by a rotation of the polarization axis. Both respond significantly differently to the applied in-plane magnetic field. Our simulations revealed that  $\text{CrCl}_3$  monolayer magnetization leads to a deterministic occupation of the  $t_{2g}$  states, leaving a hole with the orbital magnetic moment having a component along the magnetization direction. While this effect is always present, it competes with strain-induced ground-state degeneracy lifting. Further studies are needed to distinguish between the change in phonon population and phonon coupling in the strained samples and the role of magnons in the vibronic transitions.

Remarkably, our simulations found that magnetic orbital and spin moments of the hole in the  $t_{2g}$  state of the excited  $\text{Cr}^{3+}$  ion are not collinear with magnetization but have an out-of-the-plane component.

Annihilation of the hole by radiative recombination leads to the emission of a photon and (accompanied by) a magnon, required to explain the anticipated spin defect. The relaxation into the ground state also opens a channel for a loss of orbital angular momentum via the generation of orbital currents or conversion into the angular momentum of magnons and phonons, possibly mediating magnon-phonon interaction and resulting in the formation of magnon-polarons. Thus, our findings should be further explored as  $\text{CrCl}_3$  could become a model system for the heralded generation of magnons and magnon-polarons. This can be very relevant for quantum information as magnons are considered a preferred candidate for coupling between optically driven spin qubits.

### ASSOCIATED CONTENT

Supporting Information: Additional experimental details including polarization-resolved photoluminescence setup and magnetization measurement, description of energy diagram, *ab-initio* calculation details and supporting result regarding polarized emission of  $\text{CrCl}_3$ . (PDF)

### ACKNOWLEDGEMENTS

L. Z acknowledges funding from China Scholarship Council: project 20173109 within “Photo sources from two dimensional materials”. M. L acknowledges computing time on the supercomputer JURECA<sup>32</sup> at Forschungszentrum Jülich under grants no. JIFF38 and no. JIFF40. Y. M acknowledges financial support by the Deutsche Forschungsgemeinschaft (DFG, German Research Foundation) — TRR 288/2 -- 422213477 (project B06), TRR 173/3 -- 268565370 (project A11). This work was supported by the EIC Pathfinder OPEN grant 101129641 “OBELIX”. M.N. B and B.K acknowledge funding from Volkswagen Foundation, project no. 93425 within the “Integration of Molecular Components in Functional Macroscopic Systems” initiative, and R. R acknowledges funding from the Humboldt Association. We acknowledge the Helmholtz Nano Facility staff of Forschungszentrum Jülich for helping fabricate substrates.

### Notes

The authors declare no competing financial interest.

### REFERENCES

- (1). P. Němec, M. Fiebig, T. Kampfrath and A.V. Kimel. Antiferromagnetic opto-spintronics. *Nat. Phys.* 2018, **14** (3), 229-241.
- (2). D. Go, D. Jo, H.-W. Lee, M. Kläui and Y. Mokrousov. Orbitronics: Orbital currents in solids. *Europhys. Lett.* 2021, **135** (3), 37001.
- (3). M. Mostovoy. Multiferroics: different routes to magnetoelectric coupling. *npj Spintronics* 2024, **2** (1), 18.
- (4). T.S. Seifert, D. Go, H. Hayashi, R. Rouzegar, F. Freimuth, K. Ando, Y. Mokrousov and T. Kampfrath. Time-domain observation of ballistic orbital-angular-momentum currents with giant relaxation length in tungsten. *Nat. Nanotechnol.* 2023, **18** (10), 1132-1138.
- (5). T. Adamantopoulos, M. Merte, D. Go, F. Freimuth, S. Blügel and Y. Mokrousov. Orbital rashba effect as a platform for robust orbital photocurrents. *Phys. Rev. Lett.* 2024, **132** (7), 076901.
- (6). Y.-G. Choi, D. Jo, K.-H. Ko, D. Go, K.-H. Kim, H.G. Park, C. Kim, B.-C. Min, G.-M. Choi and H.-W. Lee. Observation of the orbital Hall effect in a light metal Ti. *Nature* 2023, **619** (7968), 52-56.
- (7). M. Berritta, R. Mondal, K. Carva and P.M. Oppeneer. Ab initio theory of coherent laser-induced magnetization in metals. *Phys. Rev. Lett.* 2016, **117** (13), 137203.

- (8). T. Adamantopoulos, D. Go, P.M. Oppeneer and Y. Mokrousov. Light-induced Orbital and Spin Magnetism in *3d*, *4d* and *5d* Transition Metals. arXiv preprint arXiv:2411.18815 2024.
- (9). X. Wang, J. Cao, Z. Lu, A. Cohen, H. Kitadai, T. Li, Q. Tan, M. Wilson, C.H. Lui, D. Smirnov, S. Sharifzadeh and X. Ling. Spin-induced linear polarization of photoluminescence in antiferromagnetic van der Waals crystals. *Nat. Mater.* 2021, **20** (7), 964-970.
- (10). K. Hwangbo, Q. Zhang, Q. Jiang, Y. Wang, J. Fonseca, C. Wang, G.M. Diederich, D.R. Gamelin, D. Xiao, J.H. Chu, W. Yao and X. Xu. Highly anisotropic excitons and multiple phonon bound states in a van der Waals antiferromagnetic insulator. *Nat. Nanotechnol.* 2021, **16** (6), 655-660.
- (11). F. Song, Y. Lv, Y.-J. Sun, S. Pang, H. Chang, S. Guan, J.-M. Lai, X.-J. Wang, B. Wu, C. Hu, Z. Yuan and J. Zhang. Manipulation of anisotropic Zhang-Rice exciton in NiPS<sub>3</sub> by magnetic field. *Nat. Commun.* 2024, **15** (1).
- (12). V.M. Bermudez and D.S. McClure. Spectroscopic studies of the two-dimensional magnetic insulators chromium trichloride and chromium tribromide—I. *JPCS* 1979, **40** (2), 129-147.
- (13). V.M. Bermudez and D.S. McClure. Spectroscopic studies of the two-dimensional magnetic insulators chromium trichloride and chromium tribromide—II. *JPCS* 1979, **40** (2), 149-173.
- (14). K.L. Seyler, D. Zhong, D.R. Klein, S. Gao, X. Zhang, B. Huang, E. Navarro-Moratalla, L. Yang, D.H. Cobden, M.A. McGuire, W. Yao, D. Xiao, P. Jarillo-Herrero and X. Xu. Ligand-field helical luminescence in a 2D ferromagnetic insulator. *Nat. Phys.* 2017, **14** (3), 277-281.
- (15). P.D. Fleischauer and P. Fleischauer. Photoluminescence of transition metal coordination compounds. *Chem. Rev.* 1970, **70** (2), 199-230.
- (16). Z. Zhang, J. Shang, C. Jiang, A. Rasmita, W. Gao and T. Yu. Direct Photoluminescence Probing of Ferromagnetism in Monolayer Two-Dimensional CrBr<sub>3</sub>. *Nano Lett.* 2019, **19** (5), 3138-3142.
- (17). M. Grzeszczyk, S. Acharya, D. Pashov, Z. Chen, K. Vaklinova, M. van Schilfgaarde, K. Watanabe, T. Taniguchi, K.S. Novoselov, M.I. Katsnelson and M. Koperski. Strongly Correlated Exciton-Magnetization System for Optical Spin Pumping in CrBr<sub>3</sub> and CrI<sub>3</sub>. *Adv. Mater.* 2023, **35** (17).
- (18). M.A. McGuire, G. Clark, K. Santosh, W.M. Chance, G.E. Jellison Jr, V.R. Cooper, X. Xu and B.C. Sales. Magnetic behavior and spin-lattice coupling in cleavable van der Waals layered CrCl<sub>3</sub> crystals. *Phys. Rev. Mater.* 2017, **1** (1), 014001.
- (19). X. Cai, T. Song, N.P. Wilson, G. Clark, M. He, X. Zhang, T. Taniguchi, K. Watanabe, W. Yao, D. Xiao, M.A. McGuire, D.H. Cobden and X. Xu. Atomically Thin CrCl<sub>3</sub>: An In-Plane Layered Antiferromagnetic Insulator. *Nano Lett.* 2019, **19** (6), 3993-3998.
- (20). L. Zhu and L. Yang. Quasiparticle energies and excitonic effects of chromium trichloride: From two dimensions to bulk. *Phys. Rev. B.* 2020, **101** (24).
- (21). M. Wu, Z. Li and S.G. Louie. Optical and magneto-optical properties of ferromagnetic monolayer CrBr<sub>3</sub>: A first-principles GW and GW plus Bethe-Salpeter equation study. *Phys. Rev. Mater.* 2022, **6** (1), 014008.
- (22). F. Cantos-Prieto, A. Falin, M. Alliat, D. Qian, R. Zhang, T. Tao, M.R. Barnett, E.J.G. Santos, L.H. Li and E. Navarro-Moratalla. Layer-Dependent Mechanical Properties and Enhanced Plasticity in the Van der Waals Chromium Trihalide Magnets. *Nano Lett.* 2021, **21** (8), 3379-3385.
- (23). J. Dillon Jr, H. Kamimura and J. Remeika. Magneto-optical properties of ferromagnetic chromium trihalides. *JPCS* 1966, **27** (9), 1531-1549.
- (24). M. Yamaga, B. Henderson and K. O'donnell. Polarization spectroscopy of Cr<sup>3+</sup> ions in laser host crystals: II. The broadband transitions. *J. Lumin.* 1990, **46** (6), 397-418.
- (25). G. Kresse and J. Furthmüller. Efficiency of ab-initio total energy calculations for metals and semiconductors using a plane-wave basis set - ScienceDirect. *Comput. Mater. Sci.* 1996, **6** (1), 15-50.
- (26). G. Kresse and J. Furthmüller. Efficient iterative schemes for ab initio total-energy calculations using a plane-wave basis set. *Phys. Rev. B.* 1996, **54** (16), 11169-11186.
- (27). G. Kresse and J. Hafner. Ab initiomolecular dynamics for liquid metals. *Phys. Rev. B.* 1993, **47** (1), 558-561.
- (28). G. Kresse and J. Hafner. Ab initiomolecular-dynamics simulation of the liquid-metal–amorphous-semiconductor transition in germanium. *Phys. Rev. B.* 1994, **49** (20), 14251-14269.

- (29). J. Zeisner, K. Mehlawat, A. Alfonsov, M. Roslova, T. Doert, A. Isaeva, B. Büchner and V. Kataev. Electron spin resonance and ferromagnetic resonance spectroscopy in the high-field phase of the van der Waals magnet CrCl<sub>3</sub>. *Phys. Rev. Mater.* 2020, **4** (6), 064406.
- (30). A. Narath. Low-Temperature Sublattice Magnetization Of Antiferromagnetic CrCl<sub>3</sub>. *Phys. Rev.* 1963, **131** (5), 1929-1942.
- (31). Z. Wang, M. Gibertini, D. Dumcenco, T. Taniguchi, K. Watanabe, E. Giannini and A.F. Morpurgo. Determining the phase diagram of atomically thin layered antiferromagnet CrCl<sub>3</sub>. *Nat. Nanotechnol.* 2019, **14** (12), 1116-1122.
- (32). P. Thörnig. JURECA: Data centric and booster modules implementing the modular supercomputing architecture at Jülich supercomputing centre. *Journal of large-scale research facilities JLSRF* 2021, **7**, A182-A182.

# Supporting information for Polarization of photoluminescence by optically driven orbital reconstruction in magnetically ordered CrCl<sub>3</sub>

Lanqing Zhou<sup>1,2</sup>, Marjana Ležaić<sup>3</sup>, Yuriy Mokrousov<sup>3,4</sup>, Minh N. Bui<sup>1,2</sup>, Renu Rani<sup>1,2</sup>, Detlev  
Grützmacher<sup>1,5</sup> and Beata E. Kardynał<sup>1,2\*</sup>

<sup>1</sup> Peter Grünberg Institute (PGI-9), Forschungszentrum Jülich, 52425 Jülich, Germany

<sup>2</sup> Department of Physics, RWTH Aachen University, 52074 Aachen, Germany

<sup>3</sup> Peter Grünberg Institute (PGI-1), Forschungszentrum Jülich, 52425 Jülich, Germany

<sup>4</sup> Institute of Physics, Johannes Gutenberg-University Mainz, 55128 Mainz, Germany

<sup>5</sup>Jülich-Aachen Research Alliance, Institute for Green-IT (PGI-10), Forschungszentrum Jülich and  
RWTH Aachen University, Germany

## Contents:

I. Sketch of polarization resolved photoluminescence measurement setup.

II.  ${}^4T_2 \rightarrow {}^4A_2$  luminescence of chromium trihalides

III. Computational details.

IV. Magnetization measurement.

Figure S1. Setup sketch of polarization resolved photoluminescence measurement.

Figure S2. Schematic configurational energy diagram.

Figure S3. Integrated intensity of ZPL as a function of polarization angle at 2K and 30K  
for high strain sample.

Figure S4. Variations of polarization degree and orientation in bulk samples

Figure S5. Polar plots of the vibronic peak and ZPL at different temperatures with  
dominant spin effect.

Figure S6. Temperature dependent magnetization curve.

Figure S7. Representative polar plots of the vibronic peak and ZPL with different  
external magnetic fields.

References

---

\* b.kardynał@fz-juelich.de

## I. Setup sketch of polarization resolved photoluminescence measurement.

Investigated crystals were as-purchased, cut into  $3 \times 3$  mm<sup>2</sup> flakes and fixed on SiO<sub>2</sub>/Si substrates with silver paste. Magneto-optical measurements in Voigt geometry were conducted using He-exchange gas cryostat with samples mounted on a x-y-z piezo positioner. Magnetic field was applied parallel to the CrCl<sub>3</sub> crystal monolayers while photoluminescence (PL) was excited and collected normal to the layers. The laser (at 1.8eV) beam was linearly polarized at the back-focal-plane of the objective lens which was an aspheric lens with numerical aperture of 0.75. The PL was collected by the same lens. Measurements were conducted at several positions on the samples, selected by moving the sample using an x-y-z piezo positioner. Our optical head of polarization measurement utilizes fiber coupling to deliver and collect polarized light to the Czerny–Turner spectrometer. Polarization measurements were facilitated by adding a polarization analyzer composed of linear polarizer, half waveplate and quarter waveplate in front of the optical fiber to confirm the polarization of light in incidence path. The sketch in Figure S1, half-waveplate\_2 determines the polarization direction on the sample. The rotatable half-waveplate\_3 serves as an analyzer of polarization for the emitted light. The half-waveplate\_3 and linear polarizer\_2 confirm all the light has same polarization before entering spectrometer to avoid counts difference due to sensitivity of spectrometer to polarization direction of light. A 700nm low pass filter on the input of the spectrometer was used to remove any laser light excitation.

## II. ${}^4T_2 \rightarrow {}^4A_2$ luminescence of chromium trihalides.

Chromium trihalides (CrX<sub>3</sub>) form a family of layered, insulating compounds with AFM phase at low temperatures. Each monolayer of CrX<sub>3</sub> is ordered ferromagnetically (FM), while the monolayers are coupled ferromagnetically or antiferromagnetically depending on halide atoms.<sup>33,34</sup> The octagonal crystal field of the halide ligands split d-orbitals of Cr<sup>3+</sup> into lower energy triplet and higher energy doublet.  ${}^4A_2$ , with three spin-aligned electrons occupying a low energy  $t_{2g}$  triplet of d-orbitals, is the ground state of the Cr<sup>3+</sup> ion in CrX<sub>3</sub>. The lowest energy excited state is  ${}^4T_2$ , in which one electron is lifted to  $e_g$  doublet (see the energy diagram in Figure S2).<sup>12-15</sup> In the CrI<sub>3</sub> monolayer, photoluminescence associated with the vibronic  ${}^4T_2 - {}^4A_2$  transition was found to be circularly polarized, with polarization determined by the magnetization direction. It was unpolarized in thicker layers when CrI<sub>3</sub> monolayers were AFM coupled and circularly polarized again when in FM order.<sup>14</sup> The polarization degree of the vibronic luminescence peak was used to get insight into the magnetization of CrBr<sub>3</sub>.<sup>16</sup> The coupling of the excited electron spin with the magnetization of monolayers was shown to be different in CrI<sub>3</sub> and CrBr<sub>3</sub>.<sup>17</sup>

### III. Computational details.

For electronic structure calculations, we employ Density Functional Theory (DFT) as implemented in the Vienna Ab-initio Simulation Package (VASP),<sup>25-28</sup> with Projector Augmented-Wave Method.<sup>35</sup> The cut-off energy for the plane-wave basis was set at 500eV. Perdew-Burke-Ernzerhof generalized gradient approximation revised for solids (PBEsol)<sup>36</sup> was used for the exchange and correlation. The enhanced correlation effects in Cr *d*-shell were accounted for within the DFT+U method, in Liechtenstein approach,<sup>37</sup> with the values of the screened on-site Coulomb repulsion  $U=1.79$  eV and intra-atomic exchange interaction  $J=0.85$ , as evaluated in<sup>38</sup>, within the constrained random phase approximation.<sup>39</sup> Brillouin zone was sampled on a  $5 \times 5 \times 1$  k-points mesh. Spin-orbit coupling effects are included. We simulate ferromagnetically ordered monolayer of  $\text{CrCl}_3$  in a repeated slab geometry, in a calculational unit cell containing eight formula units per monolayer and a  $\sim 20\text{\AA}$  thick vacuum region which prevents spurious interaction effects between the simulated monolayers.

### IV. Magnetization measurement.

The magnetic moment of the  $\text{CrCl}_3$  bulk crystal was measured using vibrating sample magnetometry (VSM) integrated into a Quantum Design Dynacool Physical Property Measurement System (PPMS). The sample is mounted on a rod that vibrates at a specific frequency (typically a few tens of Hz) within an in-plane magnetic field ( $H // ab$ ). This vibration induces an oscillating magnetic flux in nearby pickup coils, generating an electrical signal proportional to the sample's magnetic moment. In this technique, sample magnetization is detected as an electrical current induced in the pickup coils when sample is moving up and down along the axis of the coil. In Figure 3(j), we give the magnetic moment versus magnetic field which is consistent with two-step spin aligning process.<sup>18, 30, 31</sup> The temperature dependent magnetization curve is shown in Figure S6, there we see spike at around 14 K corresponding to antiferromagnetic ordering associated with moments alignments between two consecutive layers.<sup>40,</sup>

41

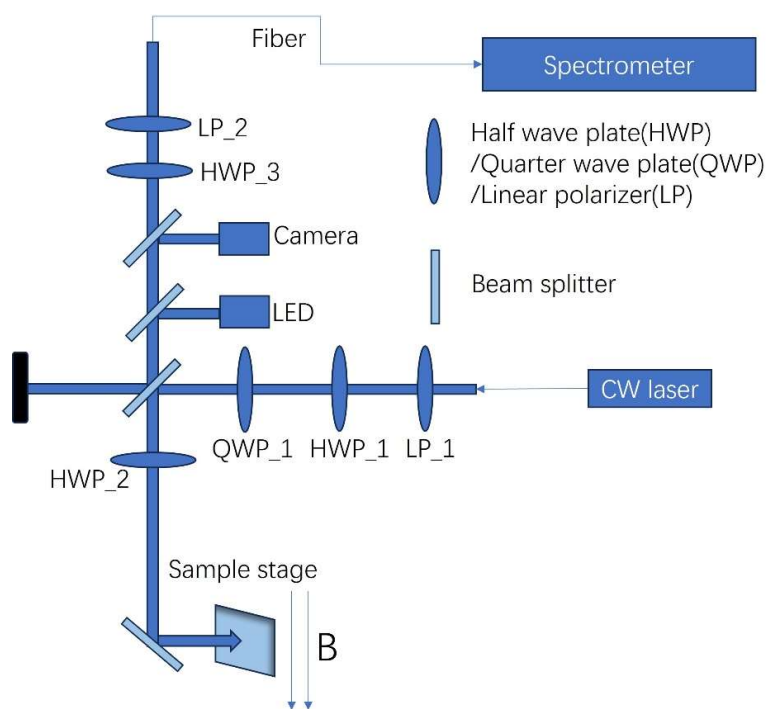


Figure S1. Setup sketch of polarization resolved photoluminescence measurement.

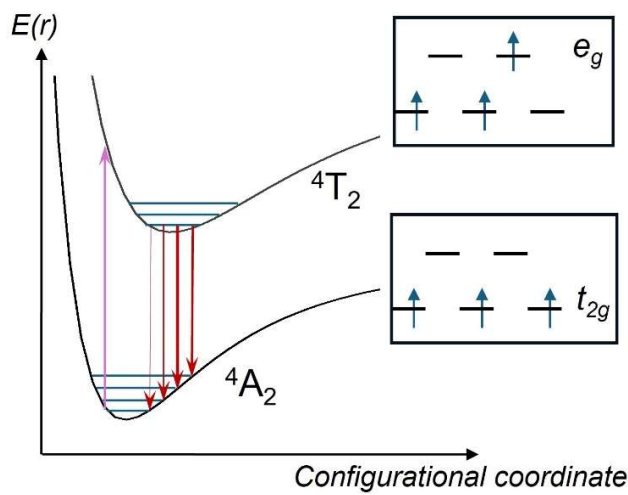


Figure S2. Schematic configurational energy diagram showing absorption (magenta arrow) and emission (red arrow). The ligand field splits the 3d orbitals into two sets,  $e_g$  and  $t_{2g}$ . At ground state, three electrons occupy three  $t_{2g}$  orbitals and one electron will promote from  $t_{2g}$  to  $e_g$  at excited state.

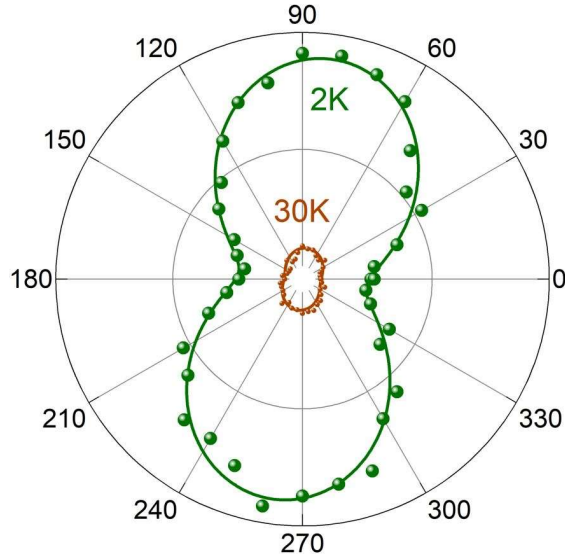


Figure S3. Integrated intensity of ZPL as a function of polarization angle at 2 K and 30 K for high strain sample, corresponding to the sample spot in Figure 2(a). The polarization direction is  $82.4^\circ$  and  $80.8^\circ$  at 2 K and 30 K.

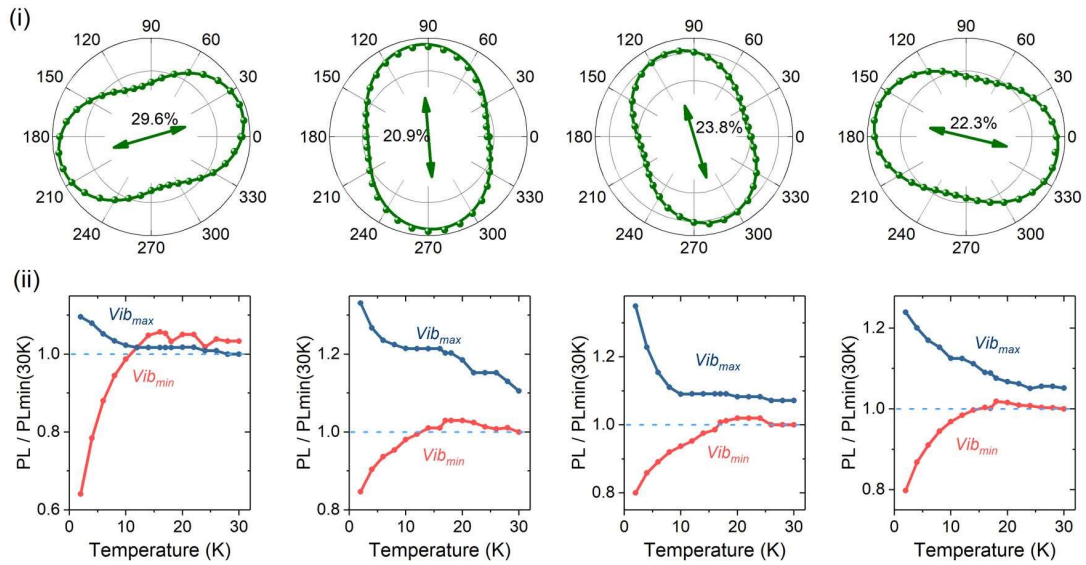


Figure S4. Variation of orientation and degree of polarization in bulk samples. Upper panel (i), polar plots of integrated counts of vibronic peak as a function of polarization angle with different orientations and degree of polarization. The arrows represent the polarization direction and the numbers above the arrow are degrees of polarization. Lower panel (ii), evolution of integrated counts corresponding to the upper polar plot at two orthogonal directions ( $Vib_{max}$  and  $Vib_{min}$ ) with temperature, divided by  $Vib_{min}$  at 30K.

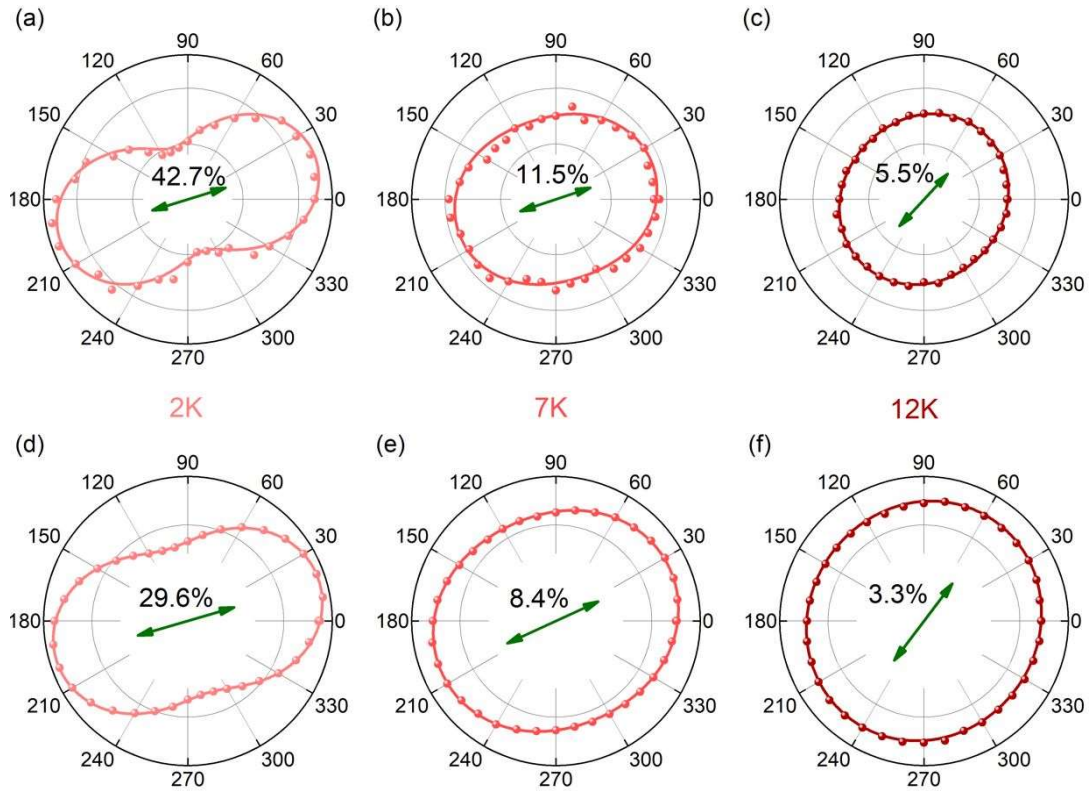


Figure S5. Polar plots of the vibronic peak and ZPL at different temperatures with dominant spin effect. Integrated counts as a function of the polarization angle at detection for ZPL in (a) to (c) and the vibronic in (d) to (f) at three temperatures 2K, 7K and 12K, measured from the same sample spot as the data in Figure 2(d). The corresponding degree of polarization is labelled above the arrow which represents polarization direction. Polar plots are with same radial scale both for vibronic peak and ZPL. Observably, there is rotation of the polarization direction when the temperature approaches Néel temperature from 2K. The orientation is  $17.1^\circ$ ,  $18.6^\circ$  and  $47.2^\circ$  at 2 K, 7 K and 12 K for ZPL and  $16.2^\circ$ ,  $24.7^\circ$  and  $52.8^\circ$  for vibronic peak. The variation of intensity and polarization degree match with Figure 2(e) and (f). The behaviors illustrate significant relevance between PL with preferred polarization and aligned spins in  $\text{CrCl}_3$ .

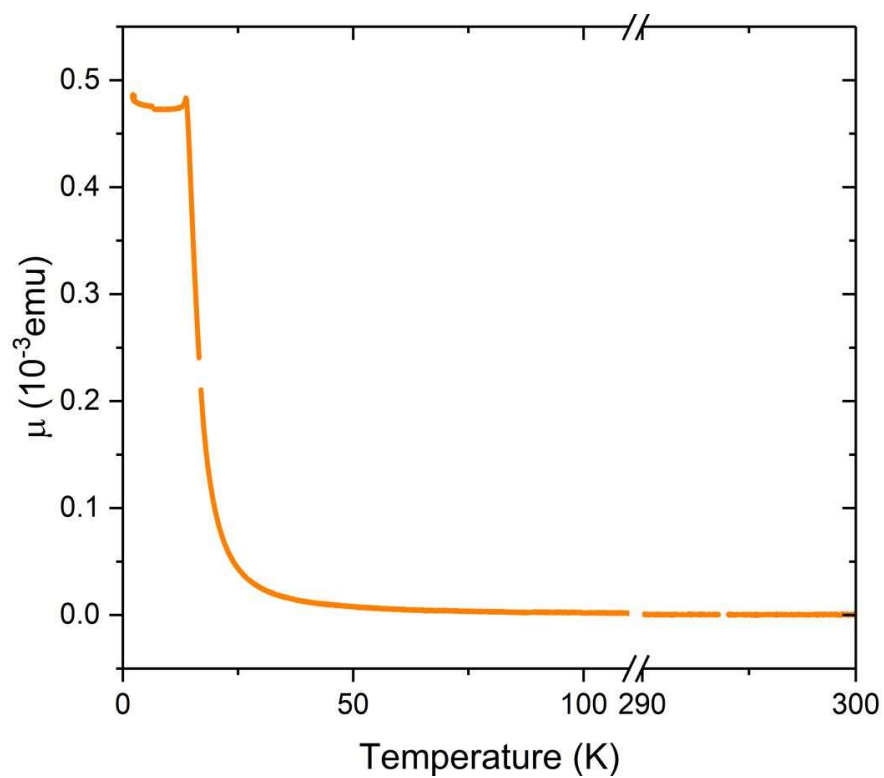


Figure S6. Temperature dependent magnetization measurement. The measurement is conducted under applied field of 50 mT along the ab-plane direction. The curve shows a spike at 14K corresponding to the antiferromagnetic ordering. The curve breaks are due to touchdown while they show negligible effects.

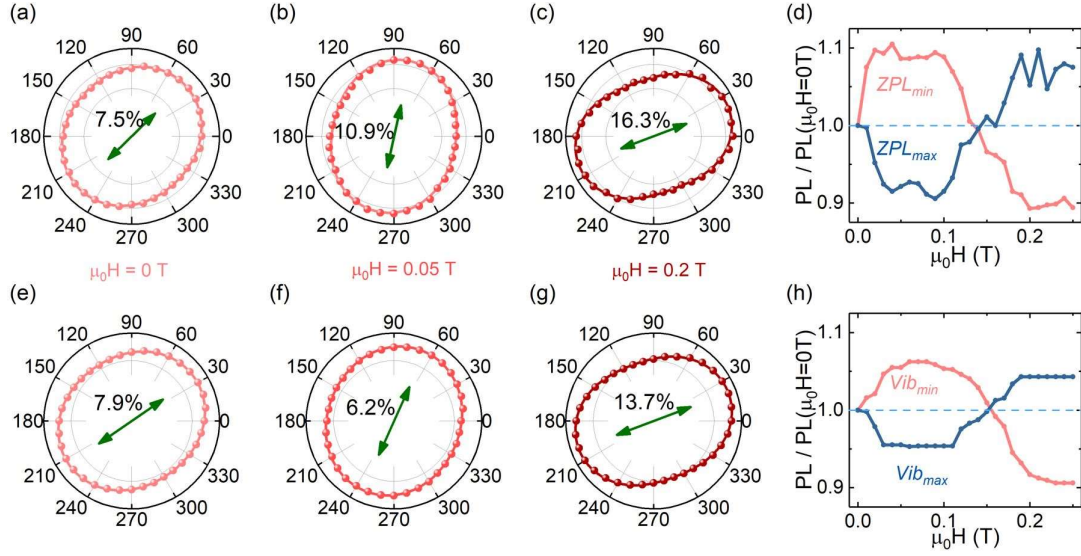


Figure S7. Representative polar plots of the vibronic signal and ZPL as a function of orientation of analyzer under different external magnetic fields for a region where polarization is extremely sensitive to temperature, similar with the one as shown in Figure 3. (a) to (d) represent polar plots with same radial scale for ZPL while (e) to (h) represent vibronic emission. The plot of normalized ZPL line/vibronic signal intensity, which are divided by intensity at zero field, as a function of magnetic field in (d) and (h) are obtained by fixing the polarization angles along (and perpendicular to) the direction of polarization at zero magnetic field. The changes of the integrated intensity result from polarization rotation and change of total intensity. The polarized direction for ZPL at 0, 0.05 and 0.2 T are  $44.2^\circ$ ,  $77.8^\circ$  and  $20.6^\circ$ . The polarized directions for vibronic emission are  $34.7^\circ$ ,  $65.9^\circ$  and  $20.6^\circ$ .

## References

- (1). P. Němec, M. Fiebig, T. Kampfrath and A.V. Kimel. Antiferromagnetic opto-spintronics. Nat. Phys. 2018, **14** (3), 229-241.
- (2). D. Go, D. Jo, H.-W. Lee, M. Kläui and Y. Mokrousov. Orbitronics: Orbital currents in solids. Europhys. Lett. 2021, **135** (3), 37001.
- (3). M. Mostovoy. Multiferroics: different routes to magnetoelectric coupling. npj Spintronics 2024, **2** (1), 18.
- (4). T.S. Seifert, D. Go, H. Hayashi, R. Rouzegar, F. Freimuth, K. Ando, Y. Mokrousov and T. Kampfrath. Time-domain observation of ballistic orbital-angular-momentum currents with giant relaxation length in tungsten. Nat. Nanotechnol. 2023, **18** (10), 1132-1138.
- (5). T. Adamantopoulos, M. Merte, D. Go, F. Freimuth, S. Blügel and Y. Mokrousov. Orbital rashba effect as a platform for robust orbital photocurrents. Phys. Rev. Lett. 2024, **132** (7), 076901.
- (6). Y.-G. Choi, D. Jo, K.-H. Ko, D. Go, K.-H. Kim, H.G. Park, C. Kim, B.-C. Min, G.-M. Choi and H.-W. Lee. Observation of the orbital Hall effect in a light metal Ti. Nature 2023, **619** (7968), 52-56.
- (7). M. Berritta, R. Mondal, K. Carva and P.M. Oppeneer. Ab initio theory of coherent laser-induced magnetization in metals. Phys. Rev. Lett. 2016, **117** (13), 137203.
- (8). T. Adamantopoulos, D. Go, P.M. Oppeneer and Y. Mokrousov. Light-induced Orbital and Spin Magnetism in  $3d$ ,  $4d$  and  $5d$  Transition Metals. arXiv preprint arXiv:2411.18815 2024.

- (9). X. Wang, J. Cao, Z. Lu, A. Cohen, H. Kitadai, T. Li, Q. Tan, M. Wilson, C.H. Lui, D. Smirnov, S. Sharifzadeh and X. Ling. Spin-induced linear polarization of photoluminescence in antiferromagnetic van der Waals crystals. *Nat. Mater.* 2021, **20** (7), 964-970.
- (10). K. Hwangbo, Q. Zhang, Q. Jiang, Y. Wang, J. Fonseca, C. Wang, G.M. Diederich, D.R. Gamelin, D. Xiao, J.H. Chu, W. Yao and X. Xu. Highly anisotropic excitons and multiple phonon bound states in a van der Waals antiferromagnetic insulator. *Nat. Nanotechnol.* 2021, **16** (6), 655-660.
- (11). F. Song, Y. Lv, Y.-J. Sun, S. Pang, H. Chang, S. Guan, J.-M. Lai, X.-J. Wang, B. Wu, C. Hu, Z. Yuan and J. Zhang. Manipulation of anisotropic Zhang-Rice exciton in NiPS<sub>3</sub> by magnetic field. *Nat. Commun.* 2024, **15** (1).
- (12). V.M. Bermudez and D.S. McClure. Spectroscopic studies of the two-dimensional magnetic insulators chromium trichloride and chromium tribromide—I. *JPCS* 1979, **40** (2), 129-147.
- (13). V.M. Bermudez and D.S. McClure. Spectroscopic studies of the two-dimensional magnetic insulators chromium trichloride and chromium tribromide—II. *JPCS* 1979, **40** (2), 149-173.
- (14). K.L. Seyler, D. Zhong, D.R. Klein, S. Gao, X. Zhang, B. Huang, E. Navarro-Moratalla, L. Yang, D.H. Cobden, M.A. McGuire, W. Yao, D. Xiao, P. Jarillo-Herrero and X. Xu. Ligand-field helical luminescence in a 2D ferromagnetic insulator. *Nat. Phys.* 2017, **14** (3), 277-281.
- (15). P.D. Fleischauer and P. Fleischauer. Photoluminescence of transition metal coordination compounds. *Chem. Rev.* 1970, **70** (2), 199-230.
- (16). Z. Zhang, J. Shang, C. Jiang, A. Rasmita, W. Gao and T. Yu. Direct Photoluminescence Probing of Ferromagnetism in Monolayer Two-Dimensional CrBr<sub>3</sub>. *Nano Lett.* 2019, **19** (5), 3138-3142.
- (17). M. Grzeszczyk, S. Acharya, D. Pashov, Z. Chen, K. Vaklinova, M. van Schilfgaarde, K. Watanabe, T. Taniguchi, K.S. Novoselov, M.I. Katsnelson and M. Koperski. Strongly Correlated Exciton-Magnetization System for Optical Spin Pumping in CrBr<sub>3</sub> and CrI<sub>3</sub>. *Adv. Mater.* 2023, **35** (17).
- (18). M.A. McGuire, G. Clark, K. Santosh, W.M. Chance, G.E. Jellison Jr, V.R. Cooper, X. Xu and B.C. Sales. Magnetic behavior and spin-lattice coupling in cleavable van der Waals layered CrCl<sub>3</sub> crystals. *Phys. Rev. Mater.* 2017, **1** (1), 014001.
- (19). X. Cai, T. Song, N.P. Wilson, G. Clark, M. He, X. Zhang, T. Taniguchi, K. Watanabe, W. Yao, D. Xiao, M.A. McGuire, D.H. Cobden and X. Xu. Atomically Thin CrCl<sub>3</sub>: An In-Plane Layered Antiferromagnetic Insulator. *Nano Lett.* 2019, **19** (6), 3993-3998.
- (20). L. Zhu and L. Yang. Quasiparticle energies and excitonic effects of chromium trichloride: From two dimensions to bulk. *Phys. Rev. B.* 2020, **101** (24).
- (21). M. Wu, Z. Li and S.G. Louie. Optical and magneto-optical properties of ferromagnetic monolayer CrBr<sub>3</sub>: A first-principles GW and GW plus Bethe-Salpeter equation study. *Phys. Rev. Mater.* 2022, **6** (1), 014008.
- (22). F. Cantos-Prieto, A. Falin, M. Alliat, D. Qian, R. Zhang, T. Tao, M.R. Barnett, E.J.G. Santos, L.H. Li and E. Navarro-Moratalla. Layer-Dependent Mechanical Properties and Enhanced Plasticity in the Van der Waals Chromium Trihalide Magnets. *Nano Lett.* 2021, **21** (8), 3379-3385.
- (23). J. Dillon Jr, H. Kamimura and J. Remeika. Magneto-optical properties of ferromagnetic chromium trihalides. *JPCS* 1966, **27** (9), 1531-1549.
- (24). M. Yamaga, B. Henderson and K. O'donnell. Polarization spectroscopy of Cr<sup>3+</sup> ions in laser host crystals: II. The broadband transitions. *J. Lumin.* 1990, **46** (6), 397-418.
- (25). G. Kresse and J. Furthmüller. Efficiency of ab-initio total energy calculations for metals and semiconductors using a plane-wave basis set - ScienceDirect. *Comput. Mater. Sci.* 1996, **6** (1), 15-50.
- (26). G. Kresse and J. Furthmüller. Efficient iterative schemes for ab initio total-energy calculations using a plane-wave basis set. *Phys. Rev. B.* 1996, **54** (16), 11169-11186.
- (27). G. Kresse and J. Hafner. Ab initiomolecular dynamics for liquid metals. *Phys. Rev. B.* 1993, **47** (1), 558-561.
- (28). G. Kresse and J. Hafner. Ab initiomolecular-dynamics simulation of the liquid-metal-amorphous-semiconductor transition in germanium. *Phys. Rev. B.* 1994, **49** (20), 14251-14269.
- (29). J. Zeisner, K. Mehawat, A. Alfonsov, M. Roslova, T. Doert, A. Isaeva, B. Büchner and V. Kataev. Electron spin resonance and ferromagnetic resonance spectroscopy in the high-field phase of the

- van der Waals magnet  $\text{CrCl}_3$ . *Phys. Rev. Mater.* 2020, **4** (6), 064406.
- (30). A. Narath. Low-Temperature Sublattice Magnetization Of Antiferromagnetic  $\text{CrCl}_3$ . *Phys. Rev.* 1963, **131** (5), 1929-1942.
- (31). Z. Wang, M. Gibertini, D. Dumcenco, T. Taniguchi, K. Watanabe, E. Giannini and A.F. Morpurgo. Determining the phase diagram of atomically thin layered antiferromagnet  $\text{CrCl}_3$ . *Nat. Nanotechnol.* 2019, **14** (12), 1116-1122.
- (32). P. Thörnig. JURECA: Data centric and booster modules implementing the modular supercomputing architecture at Jülich supercomputing centre. *Journal of large-scale research facilities JLSRF* 2021, **7**, A182-A182.
- (33). S. Yang, T. Zhang and C. Jiang. van der Waals Magnets: Material Family, Detection and Modulation of Magnetism, and Perspective in Spintronics. *Advanced Science* 2021, **8** (2), 2002488.
- (34). M. McGuire. Crystal and Magnetic Structures in Layered, Transition Metal Dihalides and Trihalides. *Crystals* 2017, **7** (5), 121.
- (35). G. Kresse and D. Joubert. From ultrasoft pseudopotentials to the projector augmented-wave method. *Phys. Rev. B.* 1999, **59** (3), 1758.
- (36). J.P. Perdew, A. Ruzsinszky, G.I. Csonka, O.A. Vydrov, G.E. Scuseria, L.A. Constantin, X. Zhou and K. Burke. Restoring the density-gradient expansion for exchange in solids and surfaces. *Phys. Rev. Lett.* 2008, **100** (13), 136406.
- (37). A. Liechtenstein, V.I. Anisimov and J. Zaanen. Density-functional theory and strong interactions: Orbital ordering in Mott-Hubbard insulators. *Phys. Rev. B.* 1995, **52** (8), R5467.
- (38). I. Solovyev. Linear response theories for interatomic exchange interactions. *J. Phys. Condens. Matter* 2024, **36** (22), 223001.
- (39). F. Aryasetiawan, M. Imada, A. Georges, G. Kotliar, S. Biermann and A. Lichtenstein. Frequency-dependent local interactions and low-energy effective models from electronic structure calculations. *Phys. Rev. B.* 2004, **70** (19), 195104.
- (40). S. Mondal, A. Midya, M.M. Patidar, V. Ganesan and P. Mandal. Magnetic and magnetocaloric properties of layered van der Waals  $\text{CrCl}_3$ . *Appl. Phys. Lett.* 2020, **117** (9).
- (41). N. Bykovetz, A. Hoser and C.L. Lin. Critical region phase transitions in the quasi-2D magnet  $\text{CrCl}_3$ . *AIP Adv.* 2019, **9** (3).